



Wide-field Fourier magnetic imaging with electron spins in diamond



Zhongzhi Guo^{1,2,6}, You Huang^{1,2,6}, Mingcheng Cai^{1,2,6}, Chunxing Li^{1,2}, Mengze Shen^{1,2}, Mengqi Wang^{1,2}, Pei Yu^{1,2}, Ya Wang^{1,2,3}, Fazhan Shi^{1,2,3,4}, Pengfei Wang^{1,2,3}✉ & Jiangfeng Du^{1,2,3,5}✉

Wide-field magnetic imaging based on nitrogen-vacancy (NV) centers in diamond has been shown the applicability in material and biological science. However, the spatial resolution is limited by the optical diffraction limit (>200 nm) due to the optical real-space localization and readout of NV centers. Here, we report the wide-field Fourier magnetic imaging technique to improve spatial resolution beyond the optical diffraction limit while maintaining the large field of view. Our method relies on wide-field pulsed magnetic field gradient encoding of NV spins and Fourier transform under pixel-dependent spatial filters. We have improved spatial resolution by a factor of 20 compared to the optical resolution and demonstrated the wide-field super-resolution magnetic imaging of a gradient magnetic field. This technique paves a way for efficient magnetic imaging of large-scale fine structures at the nanoscale.

Magnetic imaging based on nitrogen vacancy (NV) centers in diamond promises quantitative and highly sensitive detection of magnetic sources in nanoscale to microscale range^{1–5}. Based on this, wide-field NV-diamond magnetic imaging, also known as quantum diamond microscopy^{6,7}, has recently emerged as a versatile technique for microscopic magnetic imaging in a variety of applications, including solid-state devices^{8,9} and electronics^{10–12}, magnetic materials^{13–15}, biomagnetism^{16–18}, and nanoscale magnetic resonance imaging (MRI)^{19–22}. The parallel detection capability of wide-field NV microscopes makes them ideally suited for applications where multiple structural units are probed over a large area, a critical step in assessing the overall performance of materials or devices. However, while wide-field NV microscopy can provide a large field of view for magnetic imaging, the spatial resolution is constrained by the diffraction limit of the optical detection system. This limitation has hindered the development of this technique for applications related to magnetic imaging that require higher spatial resolution.

Improving the localization resolution of NV centers plays a key role in improving the spatial resolution of wide-field NV microscopy. To date, optical super-resolution imaging of NV centers is mostly based on spatial scanning technique, e.g., confocal scanning such as stimulated emission depletion (STED) and its variants^{23–25}, which are difficult to integrate into wide-field NV imaging. Single-molecule localization microscopy (SMLM), such as stochastic optical reconstruction microscopy (STORM), allows

widefield imaging for sparsely distributed NV centers in bulk diamond or nanodiamonds, but is prone to artifacts at high NV concentrations^{26–28}. Therefore, there is still no super-resolution technique that is compatible with widefield magnetic imaging, which typically uses a dense layer of NV centers as a quantum sensor.

Recently, Fourier magnetic imaging²⁹ was developed to provide a nanoscale resolution for magnetic imaging based on NV centers. Different from real-space imaging techniques, Fourier magnetic imaging utilizes magnetic field gradients to encode the spatial information of NV centers into k space. Following k -space sampling and Fourier transform, a real-space image is acquired with spatial resolution determined by the maximum k value k_{\max} : $\Delta r = |2k_{\max}|^{-1}$. In the k -space imaging method, the size of real space, i.e., the encoding field of view (FOV) F , is defined by k -sampling interval Δk : $F = |2\Delta k|^{-1}$, and the experiment acquisition time is proportional to the number of phase-encoding steps N (e.g., for one-dimensional imaging, time $\propto N = F/\Delta r = k_{\max}/\Delta k$). However, it will lead an enormous time consumption for signal acquisition in case of NV centers distributing in a wide field of view, especially with high spatial resolution requirements, because to reconstruct real-space distribution of NV centers without distortion, the k -sampling interval must be smaller enough to guarantee NV centers locating into the encoding FOV without any artifacts.

In this article, we experimentally demonstrate a method termed wide-field Fourier magnetic imaging (WFMI) to overcome the resolution

¹CAS Key Laboratory of Microscale Magnetic Resonance and School of Physical Sciences, University of Science and Technology of China, Hefei 230026, People's Republic of China. ²CAS Center for Excellence in Quantum Information and Quantum Physics, University of Science and Technology of China, Hefei 230026, People's Republic of China. ³Hefei National Laboratory, University of Science and Technology of China, Hefei 230088, People's Republic of China. ⁴School of Biomedical Engineering and Suzhou Institute for Advanced Research, University of Science and Technology of China, Suzhou 215123, People's Republic of China.

⁵School of Physics, Zhejiang University, Hangzhou 310027, People's Republic of China. ⁶These authors contributed equally: Zhongzhi Guo, You Huang, Mingcheng Cai. ✉e-mail: wpf@ustc.edu.cn; djf@ustc.edu.cn

limitations of widefield NV microscopy. In our method, we eliminate the dependence of the number of phase-encoding steps N on the size of the full FOV in Fourier magnetic imaging, by using quadrature phase encoding, reduced encoding FOV, and parallel imaging. Firstly, we use the quadrature phase encoding to determine the unique position of the NV centers. Secondly, we adopt a reduced encoding FOV to decrease experiment time consumption against the full FOV. The artifacts due to reduced-FOV-related undersampling are eliminated by using the spatial filters, which are constructed in the parallel imaging based on the camera. In the experiments, we first explore the proposed method using sparsely distributed single NV centers and achieve up to ~ 35 nm resolution. Then, we demonstrate this method in widefield magnetic imaging of a one-dimension gradient AC magnetic field using a dense layer of NV ensembles. The results show that the magnetic information could be mapped over a wide field of view with a resolution beyond the diffraction limit. Finally, we discuss the potential application of the method in nanoscale MRI, technical improvement, and future developments.

Results

Experimental setup

A schematic view of the experimental setup and principle is shown in Fig. 1a. A shallow layer of NV centers beneath the diamond surface is used as the

demonstration (see Materials and Methods for sample information). A pulsed widefield green laser and microwave field are used to initialize and manipulate the quantum state of NV centers, respectively. Two pairs of coplanar gradient microcoils are used to generate the magnetic field for sensing and a high-bandwidth uniform pulsed magnetic field gradient for phase encoding. The maximum magnetic field gradient projected to the NV centers in the central region achieves $1.5 \text{ G}\cdot\mu\text{m}^{-1}$ at 4 A current (see Supplementary Fig. 3). A camera is used for the parallel readout of NV centers as the parallel detector. As defined in parallel MRI³⁰, we define the sensitive area of a single pixel of the camera as the function of pixel shape convolving the point spread function of the optical system. The sensitive area is estimated to be 700 nm in diameter. It also equals the optical resolution under Abbe optical diffraction limit in our setup (Fig. 1b).

Quadrature phase encoding

To perform WFMI, we first implement Fourier MRI on the NV centers with quadrature phase detection³¹. The pulse sequence is shown in Fig. 1c. The NV centers are first initialized to the $|0\rangle$ state by a laser pulse and then manipulated by the spin echo pulse sequence. Between the microwave pulses, the pulsed gradient field is applied to encode the spatial information of NV centers to k space. A position-related quantum phase accumulates in

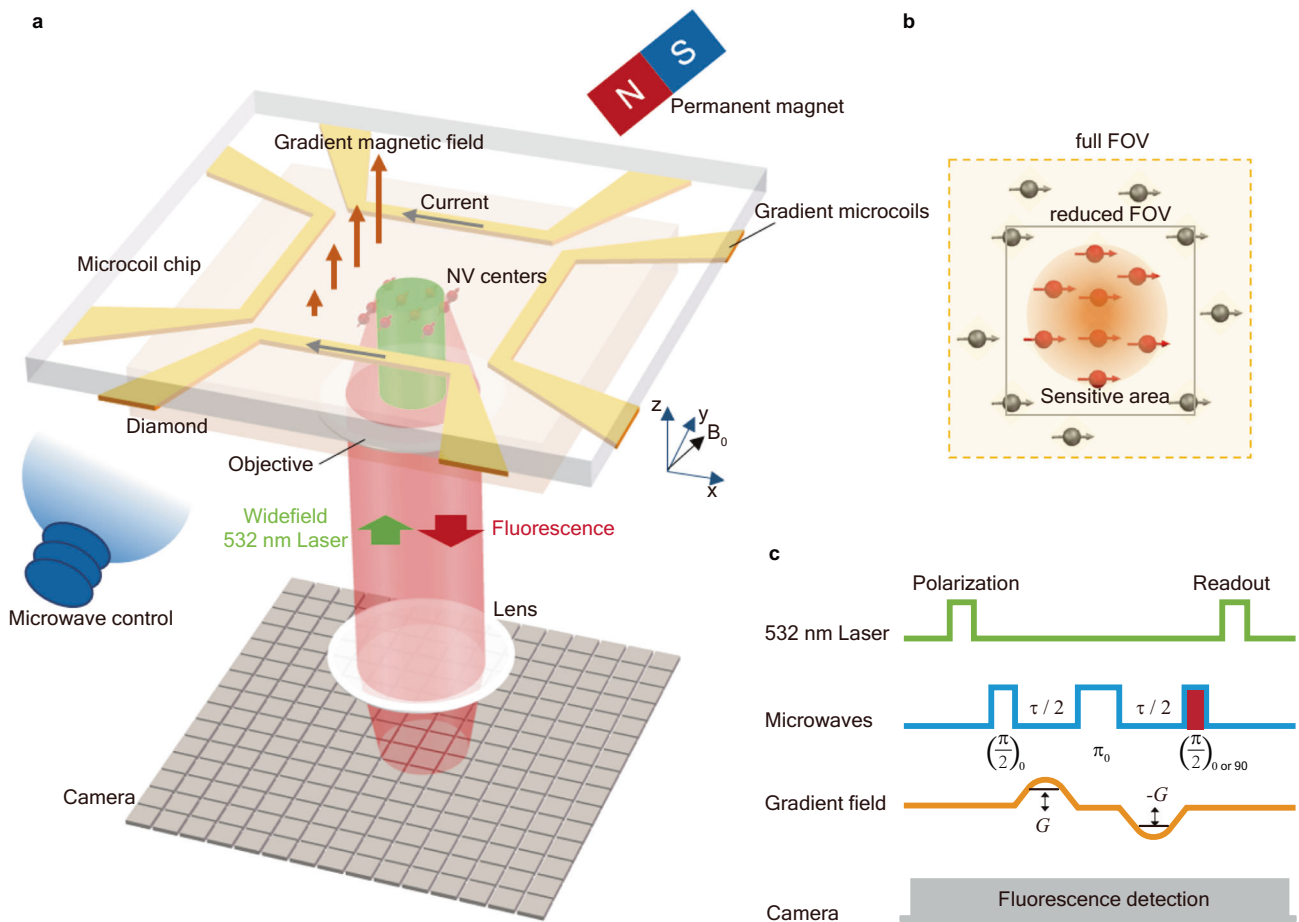


Fig. 1 | Widefield Fourier magnetic imaging (WFMI) experiment. **a** Schematic view of the experimental setup. The axial magnetic field ($B_0 \sim 340 \text{ G}$) is applied by a permanent magnet to select the NV centers with an axis lying in the x - z plane. The 532 nm excitation laser is sent into the diamond through the objective lens ($\times 60$, $\text{NA} = 0.7$), and the illuminating area forms the imaging field of view. The fluorescence is collected by the same objective lens and finally imaged on the camera. The microcoils for the generation of a pulsed gradient magnetic field are electroplated on another diamond substrate as a heat sink. **b** Schematic view of the full FOV, reduced FOV and the sensitive area of the pixel. **c** The WFMI pulse sequence with quadrature

phase detection is composed of two independent Hahn echo sequences: $(\pi/2)_0 - \tau/2 - \pi_0 - \tau/2 - (\pi/2)_0$ and $(\pi/2)_0 - \tau/2 - \pi_0 - \tau/2 - (\pi/2)_{90}$, where 0 and 90 represent microwave phases of 0° and 90° , respectively. The gradient magnetic field is turned on during free precession by sending an AC current to the microcoils, a half-cycle sinusoidal current signal is used here, and G is the time-averaged value of the gradient of the sinusoidal magnetic field during free precession. The k -space sampling is performed by incrementally stepping to vary the gradient and measuring fluorescence.

the superposition of the $|0\rangle$ and $|1\rangle$ states: $\phi = 2\pi\mathbf{k} \cdot \mathbf{r}_i$, where $\mathbf{k} = \gamma\tau(G_x, G_y)$, $\gamma = 2.8 \text{ MHz}\cdot\text{G}^{-1}$ is the NV gyromagnetic ratio and τ is the total precession time. $G_x(G_y)$ is the mean gradient strength in the $x(y)$ direction and $\mathbf{r}_i = (x_i, y_i)$ is the position of the NV center. The last $\pi/2$ pulse converts the phase information into a population on the $|0\rangle$ and $|1\rangle$ states, and the following laser pulse reads out the population on the $|0\rangle$ state. By setting the relative microwave phase of this $\pi/2$ pulse to 0° and 90° , the accumulation phase ϕ is measured at two orthogonal bases. Thus, the k -space signal can be divided into the real part $Re(\mathbf{k}) \sim [1 + \cos(2\pi\mathbf{k} \cdot \mathbf{r}_i)]/2$ and the imaginary part $Im(\mathbf{k}) \sim [1 - \sin(2\pi\mathbf{k} \cdot \mathbf{r}_i)]/2$, produced by the $(\pi/2)_0$ and $(\pi/2)_{90}$ pulses, respectively. These two parts are linearly combined to generate a complex k -space signal $S_i(\mathbf{k}) = Re(\mathbf{k}) - i^*Im(\mathbf{k}) = (1 - i)/2 + (1/2)\exp(i2\pi\mathbf{k} \cdot \mathbf{r}_i)$, which can be transformed to a real-space signal via Fourier transform: $\tilde{S}_i(\mathbf{r}) = \text{FFT}\{S_i(\mathbf{k})\} \sim \delta(\mathbf{r} - \mathbf{r}_i)$, where we omit the zero-frequency component $\delta(\mathbf{r} = 0)$. Supplementary Fig. 6 shows the result of quadrature phase detection, where a single real-space signal is obtained. The Fourier encoding FOV is determined by the k -sampling interval $F_e = |2r_{\max}| = 1/\Delta k$, and the pixel resolution is $\Delta r = 1/K$, with $K = k_{\max} - k_{\min}$ representing the size of k sampling range.

The FOV reduction and elimination of artifacts by parallel imaging

In the conventional MRI, the experiment time is linearly related to the size of the encoding FOV. Reducing the encoding FOV can speed up the experiment under a certain signal-to-noise ratio. We define the full FOV F_f as the area of laser illumination to all NV centers, and the reduced FOV F_r as the encoding FOV that is smaller than the full FOV. In the image reconstruction process, the real-space signal at each pixel location \mathbf{r} has an amplitude: $\tilde{S}(\mathbf{r}) = \sum_n S(n\Delta k) \cdot \exp(i2\pi\mathbf{r} \cdot n\Delta k/N)$, where n represents the n th k -sampling point and N is the number of phase-encoding steps. Typically, \mathbf{r} takes values in the encoding FOV, i.e., $\mathbf{r} \in \{-F_r/2, F_r/2\}$. To recover the position of the NV in the full FOV, we extend the range of \mathbf{r} to cover the full FOV: $\mathbf{r} \in \{-F_r/2 - M_1 \cdot F_r, F_r/2 + M_2 \cdot F_r\}$, where M_1, M_2 are positive integers and satisfy $(M_1 + M_2 + 1) > F_f/F_r$. In the extended FOV, the real-space signals have a periodicity: $\tilde{S}(\mathbf{r} + m \cdot F_r) = \tilde{S}(\mathbf{r})$, where m is an integer and $-M_1 \leq m \leq M_2$. Therefore, for a NV center located at \mathbf{r}_i , there will be one true signal locating at \mathbf{r}_i and multiple harmonic components (also named artifacts) at $\mathbf{r}_i + m \cdot F_r$ ($m \neq 0$) in the reconstructed image. This means encoding by the reduced FOV shortens the time consumption but causes the artifacts when we extend the reduced FOV directly to the full FOV in the Fourier transforming procedure.

Parallel imaging³⁰ is an effective way to reduce the size of encoding FOV as well as eliminate the artifacts. It employs an array of multiple radio-frequency coils to simultaneously encode spatial information and receive signals from nuclear spins. Since each coil in the array can only transmit and receive signals for the nuclear spins locating in its sensitive area, the encoding FOV can be reduced, shortening the acquisition time for MRI. Similarly, in WFMI, the camera acts as the parallel optical detector, and only the NV centers within the sensitive area contribute fluorescence to the pixel. So the camera provides the base for parallel encoding Fourier magnetic imaging of NV centers. In order to eliminate artifacts due to reduced-FOV encoding, we build the spatial filter by the sensitive area of the pixel. We set the central position of the spatial filter as the (x, y) coordinates of mapped pixel in the plane of NV centers, and the full width at half maximum (FWHM) $W = L_{\text{pixel}} + L_{\text{PSF}}$, where L_{pixel} is the size of the mapped pixel in the plane of NV centers, and L_{PSF} is the FWHM of the point spread function of the optical system. By applying the spatial filter to real-space data acquired by the pixel, the actual signal will be retained and the unique position of NV center can be recovered.

Demonstration of parallel imaging of single NV centers

In the experiment, we first use single NV centers in nanopillars as a proof-of-principle demonstration. Prior to k -space sampling, we defined the real-space coordinate system and set the origin to the position where the magnetic field B_E generated by the coil equals zero (Fig. 2a). Then we follow these procedures to obtain the image of NV centers: (1) Perform widefield Fourier imaging with the pulse sequence in Fig. 1c with reduced FOV. The phase

encoding time was set to $\tau = 10.73 \mu\text{s}$. The k sampling range in the experiment is $[-49\Delta k, 49\Delta k]$ with $\Delta k = 0.451 \mu\text{m}^{-1}$, which corresponds to a reduced FOV of $2.22 \mu\text{m}$ with a pixel resolution of 22.4 nm . In the y direction, the reduced FOV is $3.70 \mu\text{m}$ with a pixel resolution of 37.4 nm . The k -space data and its Fourier transform with a high pass filter is shown in Fig. 2b, c (Supplementary Fig. 6). (2) Subsequently, the data of the pixel corresponding to NV1 in the reduced FOV (Fig. 2c) are extended to full FOV (Fig. 2d in x and Fig. 2f in y). (3) Define and apply the spatial filter of the pixel corresponding to each NV center to eliminate the artifacts. The final location of NV1 is shown in Fig. 2e, g in x and y direction, respectively. The same results of NV2 are also shown in Fig. 2h–k. We then compared the localization results of parallel encoding Fourier imaging and widefield fluorescence imaging. In the widefield fluorescence image, the distances of NV1 and NV2 in the x and y directions are $10.39 \pm 0.05 \mu\text{m}$ and $3.96 \pm 0.02 \mu\text{m}$, respectively, while in parallel encoding Fourier imaging they are $10.52 \pm 0.03 \mu\text{m}$ and $3.81 \pm 0.03 \mu\text{m}$, respectively. This implies two results are consistent, with a remaining error maybe caused by the tiny nonlinearity of the magnetic field gradient. The FWHM of 34.3 nm appears at the y direction of NV2, corresponding to the highest resolution in this demonstration. Combining the position of NV1 and the signal peak width (Fig. 2e), the imaging spatial dynamic range (FOV/resolution) achieves 306 in this measurement. It is worth noting that the peak width of NV2 in the x direction is 190 nm , which is much larger than NV1 at 53 nm . This is due to the obvious blinking behavior of NV2 during the test, the position broadening may be brought by the fluorescence instability.

Perform parallel encoding Fourier magnetic imaging on a 2-dimensional NV layer

We next demonstrate that parallel encoding Fourier imaging can efficiently locate the ensemble NV centers in a 2D thin layer with an estimated density of $\sim 1 \times 10^{10} \text{ cm}^{-2}$. We acquired k -space data in the y direction with a k sampling range of $[-5.88, 11.88] \mu\text{m}^{-1}$ and an interval of $0.12 \mu\text{m}^{-1}$, which corresponds to a real space with a reduced FOV of $8.33 \mu\text{m}$ and a pixel resolution of 55.9 nm . Figure 3b, c show the position of the target pixels with respect to the reduced FOV, and Fig. 3d, e show the real-space data of different pixels in the y direction. As the pixel numbers varies in the y direction, the signal peak is shifted by a corresponding distance in the same direction. In pixels 40 and 46, we observed that the signals outside the reduced FOV are wrapped around to the other side, which is consistent with theoretical predictions. In addition, the shapes of the signal peak in each pixel are different, representing different NV center distributions. For adjacent pixels (Fig. 3c), we also observed that the signal peaks of the same NV centers appeared in different pixels due to overlapping sensitive area (Fig. 3e). These results indicate that the pixel of camera can be used as an effective filter for real-space signals of NV centers.

WFMI of an AC gradient magnetic field

To show that our method can acquire real-space magnetic images beyond the optical diffraction limit, we use a 2-D NV layer to perform widefield magnetic imaging of the gradient magnetic field generated by the current in gradient microcoils. The pulse sequence shown in Fig. 4a consists of a sensing part and an encoding part. The NV centers are first initialized to $|0\rangle$ state. A spin echo pulse sequence is used to sense the magnetic field. The subsequent $10 \mu\text{s}$ waiting time, much longer than the dephasing time but much shorter than the relaxation time of NV centers, causes the coherence to decay completely, leaving only the diagonal term in the density matrix. At the end of the sensing sequence, the state population on $|0\rangle$ state can be expressed as $\rho_{00} \sim 1/2[1 + \cos(2\pi\gamma\tau_1 G_y \cdot y)]$. In real space, this is a cosine fringe with a period of $|\gamma\tau_1 G_y|^{-1}$ along the y -axis. In the following, the Fourier encoding pulse sequences are implemented with a reduced FOV. Fourier encoding is used not only for imaging NV centers but also for measuring the population of NV centers. The population of NV centers is revealed in the Fourier transformed signal $\tilde{S}(y) \sim \text{abs}\{\rho_{00} \int_{-k_{\max}}^{k_{\max}} S(k) \exp(2\pi i k \cdot y) dk\}$. This results in a Fourier imaging fringe

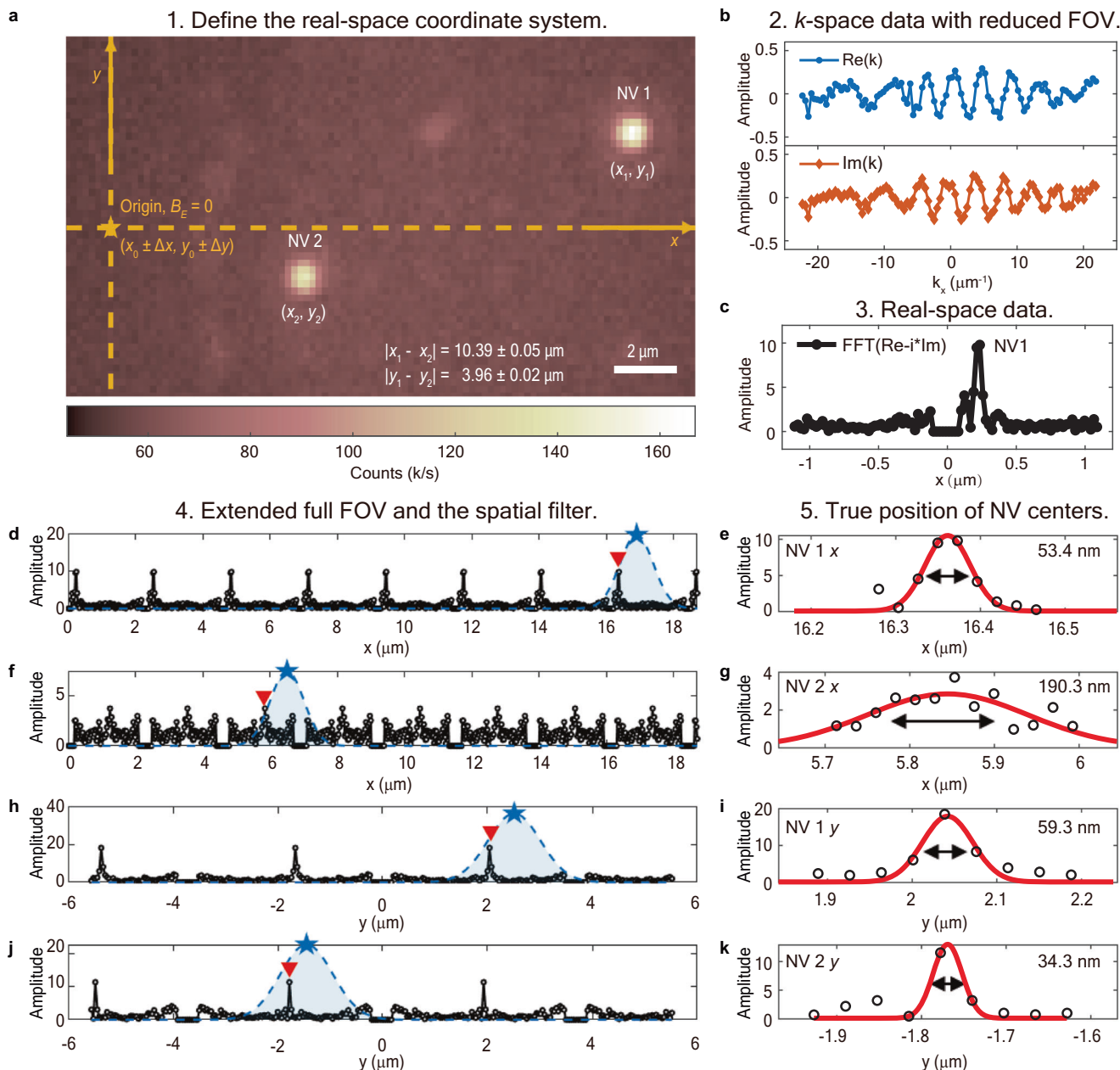


Fig. 2 | Demonstration of parallel imaging on single NV centers. **a** Widefield fluorescence image of single NV centers for defining the real-space coordinate system. The location of $B_E = 0$ (see Supplementary Fig. 3) is defined as the origin of real space (the yellow pentagram), and the direction of the gradient of the phase encoding magnetic field is defined as the x and y directions of the coordinate system (the yellow arrows in the x and y directions). The distance between NV1, NV2 and the origin is measured and listed in this image. The scale bar is 2 μm . **b** k -space data and (c) the corresponding real-space data of NV1 in the x direction in Fourier imaging with reduced FOV of 2.22 μm . **d, f, h, j** Extended full FOV for the real-space

data (black line) of NV1 and NV2 in the x and y direction, respectively. The pixel-sensitive area along with the distance between NV1 and the origin are used as the width and central position of a spatial filter (blue pentagram and shaded area formed by blue dashed line) to select the actual signal (red triangle). **e, g, i, k** x and y location measurement of NV1 and NV2 is achieved by fitting the original data using the Gaussian function, with the central position of $x_1 = 16.36 \pm 0.01 \mu\text{m}$, $y_1 = 2.04 \pm 0.01 \mu\text{m}$, $x_2 = 5.85 \pm 0.03 \mu\text{m}$, $y_2 = -1.77 \pm 0.03 \mu\text{m}$. The FWHM of each curve is shown on the upper right corner.

modulated by $|\cos(2\pi\gamma\tau_1 G_y \cdot y)|$, which has half the spacing of a wide-field fringe.

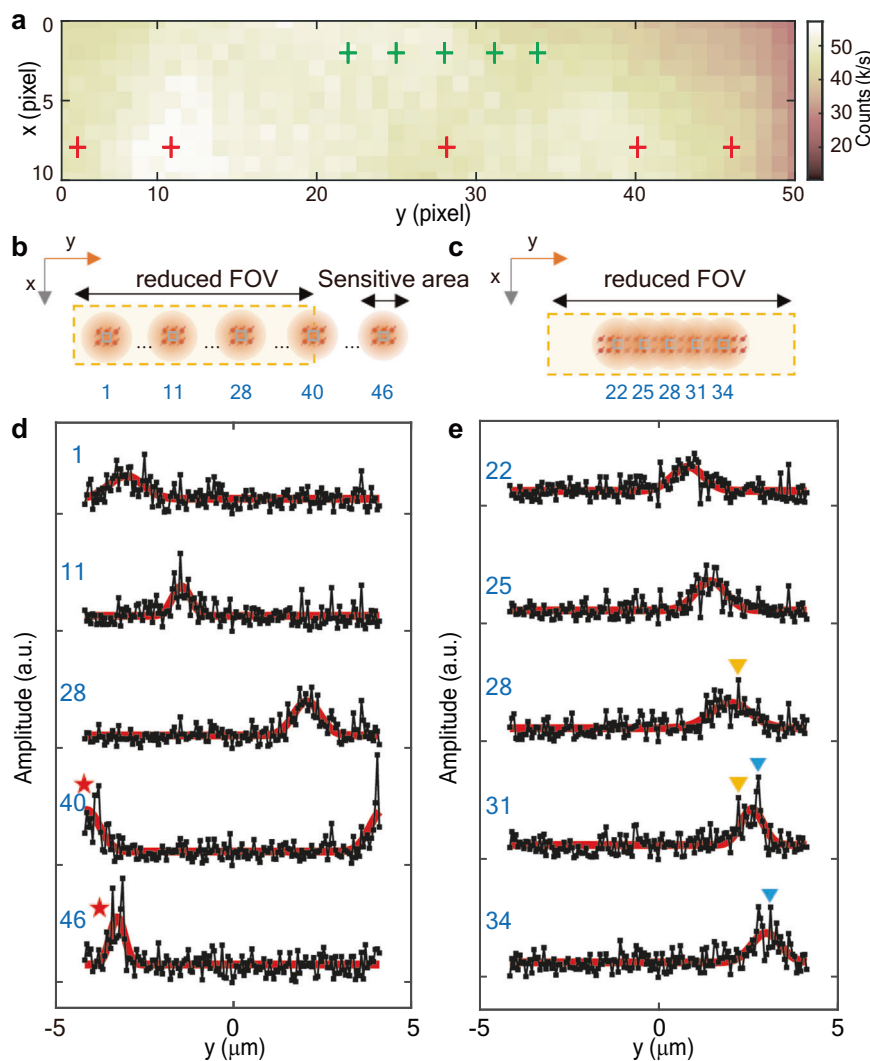
We acquired widefield and Fourier imaging fringes for three different gradient magnetic fields (Fig. 4b–j). The k sampling range is $[-2.69, 2.51] \mu\text{m}^{-1}$ in y direction, and the interval is $0.186 \mu\text{m}^{-1}$, corresponding to a real space with an encoding FOV of $5.38 \mu\text{m}$ and a resolution of 179 nm. Under the gradient value of $0.011 \text{ G}\cdot\mu\text{m}^{-1}$ and $0.099 \text{ G}\cdot\mu\text{m}^{-1}$, the Fourier imaging fringe intervals are $2.90 \mu\text{m}$ and 322 nm, respectively. As shown in Fig. 4c, when the gradient is small, the widefield fringes are visible because their spacing is larger than the diffraction limit. As the gradient rises to

$0.099 \text{ G}\cdot\mu\text{m}^{-1}$, the fringe becomes invisible in the widefield magnetic imaging because the period of the fringe is less than the optical diffraction limit (Fig. 4d, g). In the WFMI, the fringe is still visible under a pixel resolution of 179 nm. The measured Fourier imaging fringe spacing is 344 nm (Fig. 4j), which is consistent with the theoretical value.

Discussion

In this work, we proposed and experimentally demonstrated widefield Fourier magnetic imaging beyond the optical diffraction limit. All the elements needed for acquiring a magnetic image, including quadrature

Fig. 3 | Perform parallel encoding Fourier magnetic imaging on a 2-dimensional NV layer. **a** Real-space fluorescence image of the 2-D NV ensemble layer. The data of adjacent pixels (indicated by the green cross) and far-distance pixels (the red cross) are analyzed to characterize the relations between the sensitive area of the pixel and the reduced FOV. The real-space data are taken by 3×3 pixel binning for a higher signal-to-noise ratio. **b** The positional relationship of the target sensitive area inside, at the boundary, and outside the reduced FOV. The y direction is encoded and represented as a yellow arrow. **c** The positional relationship of the adjacent sensitive area of the pixel. **d** The real-space data corresponding to **b**. The center location of the signal envelope is extracted by Gaussian fitting, where $y_1 = -3.01 \pm 0.14 \mu\text{m}$, $y_{11} = -1.45 \pm 0.08 \mu\text{m}$, $y_{28} = 2.07 \pm 0.07 \mu\text{m}$, $y_{40} = -4.09 \pm 0.08 \mu\text{m}$, and $y_{46} = -3.25 \pm 0.05 \mu\text{m}$, respectively. The signals outside the reduced FOV in pixels 40 and 46 are folded to the other side and indicated by a red pentagram, and the real location can be recovered by panning to the right by the size of one encoding FOV. **e** The real-space data corresponding to **c**. The center location is measured as $y_{22} = 0.80 \pm 0.12 \mu\text{m}$, $y_{25} = 1.43 \pm 0.10 \mu\text{m}$, $y_{28} = 1.99 \pm 0.13 \mu\text{m}$, $y_{31} = 2.59 \pm 0.07 \mu\text{m}$, and $y_{34} = 2.98 \pm 0.10 \mu\text{m}$, respectively, and the mean distance of signal peaks at adjacent pixels is 546 nm. As a comparison, the distance between adjacent pixels is 585 nm. Signal peaks of the same NV centers appear in the real-space signals of adjacent pixels because of FOV overlapping, such as pixels 28, 31, and 34 (blue and yellow triangles). The mean peak width of all signal envelopes in **d** and **e** is 761 nm, representing the size of the sensitive area of the pixel.



phase detection, parallel encoding, and real-space image reconstruction, are developed and integrated with quantum sensing. It breaks through the optical diffraction limit in widefield magnetic imaging and provides a feasible method for two-dimensional high-spatial-dynamic-range magnetic imaging with the spatially multiplexed detection advantage of Fourier imaging. Furthermore, the spatial dynamic range can be improved by using large-area laser illumination and a magnetic field gradient but not by increasing the number of phase-encoding steps. In addition, conventional MRI algorithms can be introduced to reduce the number of phase-encoding steps and the imaging time, e.g., the compressed sensing technique³² and parallel imaging algorithm such as sensitivity encoding (SENSE)³³.

Our pulse sequence combines quantum sensing and Fourier encoding. It enables not only AC magnetic field imaging demonstrated in this work, but also magnetic resonance imaging applications by replacing the quantum sensing sequence with an XY-8 or double-electron-electron-resonance sequence for detecting nuclear and electron spins. Other potential applications include imaging of magnetic domains and currents in 2D magnetic materials³⁴, magnetic imaging of biological cells and tissues (e.g., neural networks), electrical characterization in microelectronics⁸ and nanoelectronics³⁵, and highly efficient detection of electronic and nuclear spin qubits inside diamond³⁶. With our protocol, magnetic imaging with millimeter FOV and nanometer resolution is within reach under the further careful design of the ultrapure NV sensor³⁷ and the magnetic field gradient.

Methods

Diamond sample preparation

All the NV centers used in this work are generated by ion implantation and followed by 1000 °C annealing under ultrahigh vacuum. The ensemble NV centers are generated by $^{14}\text{N}^+$ ion implantation into the $\langle 100 \rangle$ surface of $3 \times 3 \times 0.5$ mm HPHT ultrapure diamond. The dose and energy are $1 \times 10^{12} \text{ cm}^{-2}$ and 40 keV, respectively. The typical ensemble decoherence time is $T_2 = 11.6 \mu\text{s}$. The single NV centers are generated by $^{15}\text{N}^+$ ion implantation into the 100 surface of $2 \times 2 \times 0.1$ mm ultrapure CVD diamond, whereas the dose and energy are $1 \times 10^{10} \text{ cm}^{-2}$ and 5 keV, respectively. The NV centers are located in nanopillar array with a spacing of $2 \mu\text{m}$. The decoherence time of single NV centers in experiment is $T_2 = 9.7 \mu\text{s}$.

Gradient microcoils preparation

Gradient microcoils are fabricated by electroplating metal electrodes on a polycrystal diamond substrate with the size of $1 \text{ cm} \times 1 \text{ cm} \times 0.5 \text{ mm}$ and thermal conductivity of $1800 \text{ W} \cdot \text{m}^{-1} \cdot \text{k}^{-1}$ (Hebei Plasma Diamond). First, 20 nm Ti and 200 nm Au adhesion layers are made by magnetron sputtering. Then photolithography is performed using the exposure mode of MA6 (AZ4620, $4000 \text{ r} \cdot \text{min}^{-1}$ for 30 s and 100°C for 3 min). After that, the 3 μm Cu and 200 nm Au electrodes are deposited by electroplating, and then stripped with acetone isopropanol for 10 min each and etched by reactive ion etching (RIE) for 16 min. The final electrode layer material was Ti/Au/Cu/Au with a thickness of 20/200/3000/200 nm and a width of 10 μm . Electroplating electrodes form a square area of $100 \times 100 \mu\text{m}^2$. The square

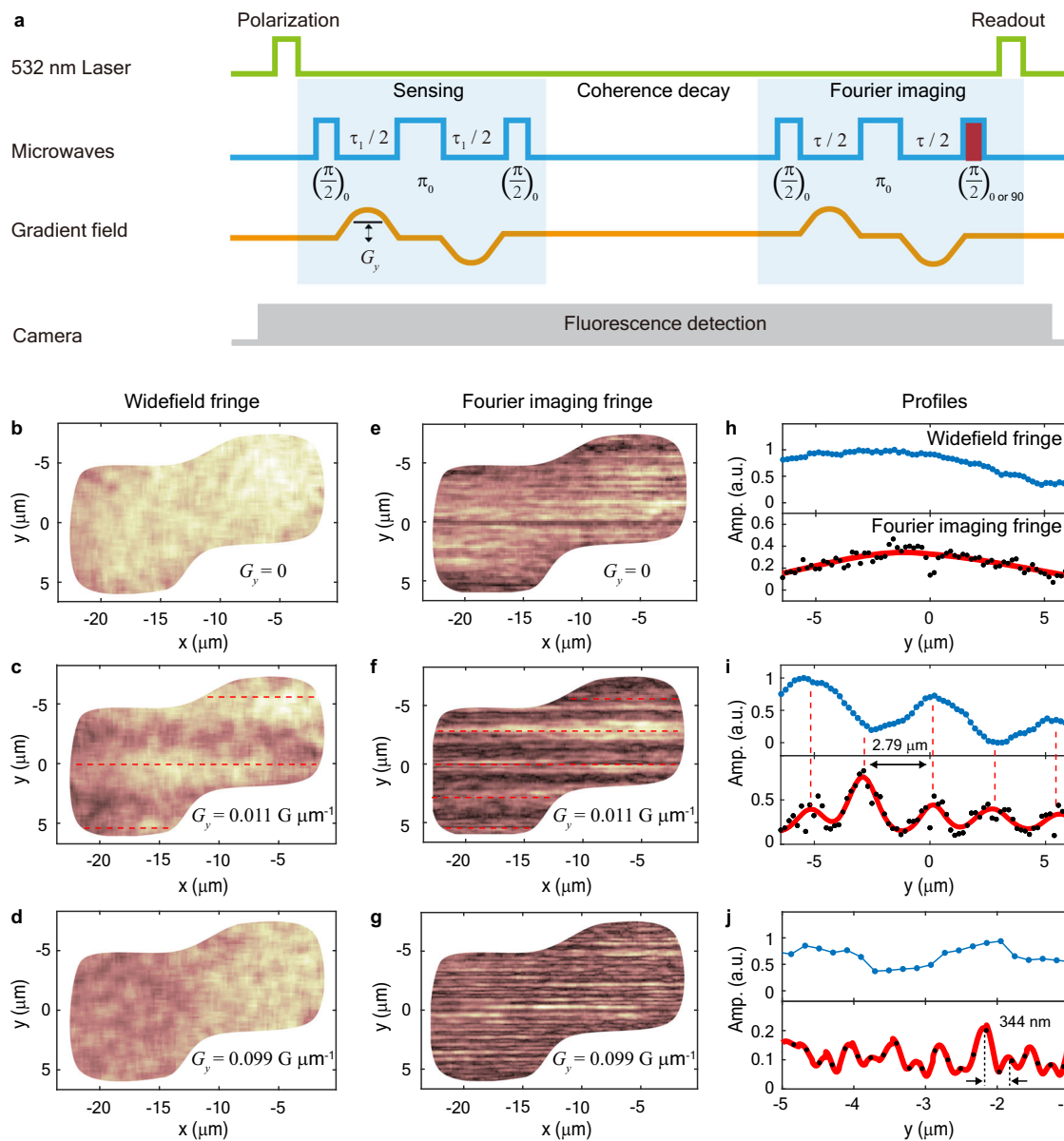


Fig. 4 | WFMI of an AC gradient magnetic field. **a** Pulse sequences of WFMI, which consists of three parts: quantum sensing, coherence decay, and Fourier imaging. An AC current with a period of 5 μ s is sent to the gradient microcoils in the y direction, which generates a magnetic field with a uniform gradient in the imaging area. The Hahn echo sequence with free precession time $\tau_1 = 5.6 \mu$ s is applied in the sensing period. **b–d** Widefield real-space imaging of the alternating gradient magnetic field

when Fourier imaging is not introduced in **a**. The different magnetic gradients are listed in these figures. **e–g** The WFMI of the alternating gradient magnetic field.

h–j The profiles in y direction taken by averaging all the pixels in each corresponding row of x direction. The blue lines are connections of the data points, and the red curves are fitting by smoothing for **h**, multiple Gaussian functions for **i**, and fast Fourier transform with zero padding for **j**.

area is then shielded by a silicon oxide-titanium-silicon oxide film with the thickness of 400/200/100 nm. The shielding layers serve to isolate the scattered light from the metal electrode and the fluorescence of impurities in the diamond substrate from the fluorescence of the NV centers in diamond sample.

Gradient magnetic field generating

In the experiment, gradient magnetic field in x and y direction are generated by two independent circuits. For each circuit, the arbitrary waveform signals are generated by an arbitrary waveform generator (AWG, Keysight, 33522B). The current signal is then amplified by a water-cooled voltage-controlled current sources (customized, VCCS, maximum output current 5 A). The amplified current is sent into the gradient microcoils to generate gradient magnetic field in the target area, with uniform gradient along the x or y direction. In order to reduce the

reflection of the current, each gradient microcoils is connected in parallel with a 51 Ω resistor. To accurately measure the k value, a 0.1 Ω high-accuracy-low-thermal-drift sampling resistor is connected in series to the gradient microcoils, and then the voltage waveform of the sampling resistor is recorded by an oscilloscope (Rigol, DS1104Z). The other channels of the oscilloscope are connected to the microwave sequence and triggering signal of camera exposure to monitor the experimental sequence in real time.

Data analysis

In the experiments of the single NV centers and ensemble NV centers, the k -space data is directly transformed to real space via Fourier transform. The real-space data is fitted by a Gaussian function to read out the peak position and full width at half maximum. In Fig. 2, the real-space data are further processed by high-pass filtering to eliminate low-frequency noise caused by

drift (Fig. S6). In the experiment of mapping gradient magnetic field, the k -space data is multiplied by Hanning window to suppress energy leakage before Fourier transform, and when performing Fourier transform, the length of the k -space data is extended to 1024 by adding 0 to the end of the experimental data. When computing the k -space data, pixel binning (3×3 for ensemble NV centers imaging and 5×5 for gradient magnetic field mapping) is used to improve the signal-to-noise ratio. For each pixel, the peak positions and intensities of the real-space data are extracted. Finally, a hybrid parallel Fourier image of NV centers is formed by assigning the x -coordinate of the pixel to the x position of the image, the peak position of real-space signal to the y position, and the peak intensity to the displayed amplitude.

Data availability

The authors declare that the data supporting the findings of this study are available within the paper and its Supplementary Information. The original data are available at <https://doi.org/10.6084/m9.figshare.25047509>.

Code availability

All codes that support the findings of this study are available from the corresponding author upon reasonable request.

Received: 2 June 2023; Accepted: 5 February 2024;

Published online: 21 February 2024

References

1. Maze, J. R. et al. Nanoscale magnetic sensing with an individual electronic spin in diamond. *Nature* **455**, 644–647 (2008).
2. Balasubramanian, G. et al. Nanoscale imaging magnetometry with diamond spins under ambient conditions. *Nature* **455**, 648–651 (2008).
3. Grinolds, M. S. et al. Quantum control of proximal spins using nanoscale magnetic resonance imaging. *Nat. Phys.* **7**, 687–692 (2011).
4. Shi, F. et al. Single-protein spin resonance spectroscopy under ambient conditions. *Science* **347**, 1135–1138 (2015).
5. Staudacher, T. et al. Nuclear magnetic resonance spectroscopy on a (5-nanometer)3 sample volume. *Science* **339**, 561–563 (2013).
6. Scholten, S. C. et al. Widefield quantum microscopy with nitrogen-vacancy centers in diamond: Strengths, limitations, and prospects. *J. Appl. Phys.* **130**, 150902 (2021).
7. Edlyn, V. & Levinea et al. Principles and techniques of the quantum diamond microscope. *Nanophotonics* **8**, 1945–1973 (2019).
8. Turner, M. J. et al. Magnetic field fingerprinting of integrated-circuit activity with a quantum diamond microscope. *Phys. Rev. Appl.* **14**, 014097 (2020).
9. Scholten, S. C. et al. Imaging current paths in silicon photovoltaic devices with a quantum diamond microscope. *Phys. Rev. Appl.* **18**, 014041 (2022).
10. Wang, E.-H. et al. Directly revealing the electrical annealing of nanoscale conductive networks with solid spins. *Appl. Phys. Lett.* **122**, 104002 (2023).
11. Ku, M. J. H. et al. Imaging viscous flow of the Dirac fluid in graphene. *Nature* **583**, 537–541 (2020).
12. Tetienne, J.-P. et al. Quantum imaging of current flow in graphene. *Sci. Adv.* **3**, e1602429 (2017).
13. Hsieh, S. et al. Imaging stress and magnetism at high pressures using a nanoscale quantum sensor. *Science* **366**, 1349–1354 (2019).
14. Lesik, M. et al. Magnetic measurements on micrometer-sized samples under high pressure using designed NV centers. *Science* **366**, 1359–1362 (2019).
15. Broadway, D. A. et al. Imaging domain reversal in an ultrathin Van der waals ferromagnet. *Adv. Mater.* **32**, 2003314 (2020).
16. Le Sage, D. et al. Optical magnetic imaging of living cells. *Nature* **496**, 486–489 (2013).
17. Glenn, D. R. et al. Single-cell magnetic imaging using a quantum diamond microscope. *Nat. Methods* **12**, 736–738 (2015).
18. Chen, S. et al. Immunomagnetic microscopy of tumor tissues using quantum sensors in diamond. *Proc. Natl Acad. Sci. USA* **119**, e2118876119 (2022).
19. DeVience, S. J. et al. Nanoscale NMR spectroscopy and imaging of multiple nuclear species. *Nat. Nanotechnol.* **10**, 129–134 (2015).
20. Simpson, D. A. et al. Electron paramagnetic resonance microscopy using spins in diamond under ambient conditions. *Nat. Commun.* **8**, 458 (2017).
21. Davis, H. C. et al. Mapping the microscale origins of magnetic resonance image contrast with subcellular diamond magnetometry. *Nat. Commun.* **9**, 131 (2018).
22. Ziem, F., Garsi, M., Fedder, H. & Wrachtrup, J. Quantitative nanoscale MRI with a wide field of view. *Sci. Rep.* **9**, 12166 (2019).
23. Rittweger, E., Han, K. Y., Irvine, S. E., Eggeling, C. & Hell, S. W. STED microscopy reveals crystal colour centres with nanometric resolution. *Nat. Photon.* **3**, 144–147 (2009).
24. Wildanger, D., Maze, J. R. & Hell, S. W. Diffraction unlimited all-optical recording of electron spin resonances. *Phys. Rev. Lett.* **107**, 017601 (2011).
25. Storterboom, J., Barbiero, M., Castelletto, S. & Gu, M. Ground-state depletion nanoscopy of nitrogen-vacancy centres in nanodiamonds. *Nanoscale Res. Lett.* **16**, 44 (2021).
26. Pfender, M., Aslam, N., Waldherr, G., Neumann, P. & Wrachtrup, J. Single-spin stochastic optical reconstruction microscopy. *Proc. Natl. Acad. Sci. USA* **111**, 14669–14674 (2014).
27. Gu, M., Cao, Y., Castelletto, S., Kouskousis, B. & Li, X. Super-resolving single nitrogen vacancy centers within single nanodiamonds using a localization microscope. *Opt. Express* **21**, 17639–17646 (2013).
28. Barbiero, M. et al. Nanoscale magnetic imaging enabled by nitrogen vacancy centres in nanodiamonds labelled by iron–oxide nanoparticles. *Nanoscale* **12**, 8847–8857 (2020).
29. Arai, K. et al. Fourier magnetic imaging with nanoscale resolution and compressed sensing speed-up using electronic spins in diamond. *Nat. Nanotechnol.* **10**, 859–864 (2015).
30. Katscher, U. & Bornert, P. Parallel magnetic resonance imaging. *Neurother.* **4**, 499–510 (2007).
31. Becker, E. D. *High Resolution NMR (Third Edition)* (ed Becker E. D.) 49–82 (Academic Press, 2000).
32. Candes, E. J., Romberg, J. & Tao, T. Robust uncertainty principles: exact signal reconstruction from highly incomplete frequency information. *IEEE Trans. Inf. Theory* **52**, 489–509 (2006).
33. Pruessmann, K. P., Weiger, M., Scheidegger, M. B. & Boesiger, P. SENSE: sensitivity encoding for fast MRI. *Magn. Reson. Med.* **42**, 952–962 (1999).
34. Casola, F., van der Sar, T. & Yacoby, A. Probing condensed matter physics with magnetometry based on nitrogen-vacancy centres in diamond. *Nat. Rev. Mater.* **3**, 17088 (2018).
35. Das, S. et al. Transistors based on two-dimensional materials for future integrated circuits. *Nat. Electron.* **4**, 786–799 (2021).
36. Cujia, K. S., Herb, K., Zopes, J., Abendroth, J. M. & Degen, C. L. Parallel detection and spatial mapping of large nuclear spin clusters. *Nat. Commun.* **13**, 1260 (2022).
37. Balasubramanian, G. et al. Ultralong spin coherence time in isotopically engineered diamond. *Nat. Mater.* **8**, 383–387 (2009).

Acknowledgements

We thank Professor J. Wen and Professor D. Liang for helpful discussions. We thank Dr. F. Yu for the development of voltage-controlled current source. This work was supported by the National Natural Science Foundation of China (Grants No. T2125011), National Natural Science Foundation of China (Grants No. 12104447), National Natural Science Foundation of China (Grants No. 92265204), National Key R&D Program of China (Grant No. 2018YFA0306600), Chinese Academy of Sciences (Grants No. ZDZBGCH2021002), Chinese

Academy of Sciences (Grants No. GJJSTD20200001), Chinese Academy of Sciences (Grants No. YSBR-068), Innovation Program for Quantum Science and Technology (Grant No. 2021ZD0303204), Innovation Program for Quantum Science and Technology (Grant No. 2021ZD0302200), and Anhui Initiative in Quantum Information Technologies and the Fundamental Research Funds for the Central Universities.

Author contributions

J.D. and P.W. proposed the idea and supervised the experiments. P.W., Z.G., M.C., Y.H., and C.L. prepared the experimental setups. Z.G. and M.C. performed the experiments. Z.G. and M.S. performed the simulation. P.Y., Y.H., and M.W. prepared the sample. C.L. designed the microwave waveguide. P.W., Z.G., and M.C. wrote the paper. All authors analyzed the data, discussed the results, and commented on the final manuscript.

Competing interests

The authors declare no competing interests.

Additional information

Supplementary information The online version contains supplementary material available at <https://doi.org/10.1038/s41534-024-00818-9>.

Correspondence and requests for materials should be addressed to Pengfei Wang or Jiangfeng Du.

Reprints and permissions information is available at <http://www.nature.com/reprints>

Publisher's note Springer Nature remains neutral with regard to jurisdictional claims in published maps and institutional affiliations.

Open Access This article is licensed under a Creative Commons Attribution 4.0 International License, which permits use, sharing, adaptation, distribution and reproduction in any medium or format, as long as you give appropriate credit to the original author(s) and the source, provide a link to the Creative Commons licence, and indicate if changes were made. The images or other third party material in this article are included in the article's Creative Commons licence, unless indicated otherwise in a credit line to the material. If material is not included in the article's Creative Commons licence and your intended use is not permitted by statutory regulation or exceeds the permitted use, you will need to obtain permission directly from the copyright holder. To view a copy of this licence, visit <http://creativecommons.org/licenses/by/4.0/>.

© The Author(s) 2024